HHS Public Access

Author manuscript

Neuroimage. Author manuscript; available in PMC 2018 November 01.

Published in final edited form as:

Neuroimage. 2017 November 01; 161: 104–119. doi:10.1016/j.neuroimage.2017.08.004.

DIRECT DETECTION OF NEURAL ACTIVITY IN VITRO USING MAGNETIC RESONANCE ELECTRICAL IMPEDANCE TOMOGRAPHY (MREIT)

Rosalind. J. Sadleir, Ph.D.[∞,¶], **Fanrui Fu, B.Sc.**[∞], **Corey. Falgas, M.Sc.**[‡], **Stephen Holland, M. Sc**[‡], **May. Boggess, Ph.D**[*], **Samuel. C. Grant, Ph.D.**[‡], and **Eung Je Woo, Ph.D.**[§]

[∞]School of Biological and Health Systems Engineering, Arizona State University, 500 E. Tyler Mall, Tempe AZ 85287-9709, USA

[‡]Department of Chemical and Biomedical Engineering, Florida A&M University-Florida State, University College of Engineering, 2525 Pottsdamer Street, Tallahassee, FL 32310, USA

[*]School of Mathematical and Statistical Sciences, Arizona State University, 901 S. Palm Walk, Tempe, AZ 85287-1804, USA

[§]Dept. of Biomedical Engineering, College of Medicine, Kyung Hee University, 23 Kyungheedae-ro, Dongdaemun-gu, Seoul 02447, Korea

Abstract

We describe a sequence of experiments performed *in vitro* to verify the existence of a new magnetic resonance imaging contrast — Magnetic Resonance Electrical Impedance Tomography (MREIT) —sensitive to changes in active membrane conductivity. We compared standard deviations in MREIT phase data from spontaneously active *Aplysia* abdominal ganglia in an artificial seawater background solution (ASW) with those found after treatment with an excitotoxic solution (KCl). We found significant increases in MREIT treatment cases, compared to control ganglia subject to extra ASW. This distinction was not found in phase images from the same ganglia using no imaging current. Further, significance and effect size depended on the amplitude of MREIT imaging current used. We conclude that our observations were linked to changes in cell conductivity caused by activity. Functional MREIT may have promise as a more

[¶]Corresponding Author: Rosalind Sadleir, Ph.D., School of Biological and Health Systems Engineering, Arizona State University, Box 879709, Tempe AZ, USA, Phone: (480) 727 9790, Fax: (480) 727 7624, rsadleir@asu.edu.

Disclosure: The authors report no conflicts of interest.

AUTHOR CONTRIBUTIONS

RJS: Designed research, performed research, analyzed data, wrote paper
FF: Performed research, analyzed data
CF and **SH:** Performed research
MB: Analyzed data, wrote paper
SG: Designed research, performed research, developed experimental platform
EW: Designed research, contributed materials.

direct method of functional neuroimaging than existing methods that image correlates of blood flow such as BOLD fMRI.

Graphical abstract

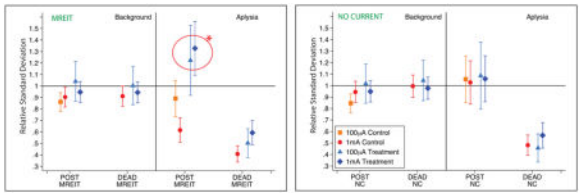

Keywords

MREIT; *Aplysia*; action potential; MRI; microelectrode array; fMRI

1. INTRODUCTION

Direct methods for functional neural imaging are critical to advancements in understanding neural behavior, plasticity, connectivity and pathology. Many methods have sought to directly image neural activity *in vivo* using magnetic resonance methods. These include the area of neural current magnetic resonance imaging (ncMRI), where disturbances in the main magnetic field of an MR system caused by intrinsic neural currents have been observed to produce artifacts in magnitude or phase images (Bandettini et al., 2005; Huang, 2014; Huang and Zhu, 2015; Jiang et al., 2014; Luo and Gao, 2009; Park et al., 2006; Petridou et al., 2006; Sundaram et al., 2016). More recently, attempts have been made to detect the effects of ion flow using Lorentz force imaging (Pourtaheri et al., 2013; Truong et al., 2008) and Mg enhanced MR imaging (Radecki et al., 2014). All these contrasts typically produce changes near or below noise floors of high field systems and require creative strategies for their recovery. The largest ncMRI signals are predicted to occur in coherent white matter (Huang and Zhu, 2015), however complex neural architecture may cause loss of signal due to self-cancellation of multiple overlapping neural current fields (Cassarà et al., 2008).

We examined Magnetic Resonance Electrical Impedance Tomography (MREIT) to determine if this approach has potential to detect neural activity. MREIT, which is sensitive to conductivity contrast (a scalar), involves administration of external currents to probe conductivity properties. In the case of neural activity, MREIT may be able to detect changes in membrane conductance associated with neural spiking (functional MREIT, fMREIT) in a similar manner to the related technique of fast neural electrical impedance tomography (Aristovich et al. 2016, Vongerichten et al. 2016). While the contrast mechanisms of fMREIT and fast neural EIT are the same, fMREIT has the advantage that signals from deep cortical structures can potentially be recovered, and implanted electrodes need not be used. MREIT signal size can be controlled by changing imaging current, so this strategy allows acquisitions to be tailored to different imaging environments. Moreover, because conductivity contrast is scalar, the method should be less sensitive to neural magnetic field architecture, potentially offering a direct functional imaging method that is robust to scaling.

In MREIT, small external currents are applied to an object as MR imaging is performed. The magnetic flux density changes caused by this current flow are encoded in MR phase data. Reconstructed phase data is then converted to conductivity or current density slice images (Seo and Woo, 2014; Seo et al., 2003; Woo and Seo, 2008). The large (ca. thirtyfold) changes in membrane conductance that occur during neural activity also cause changes in paths of externally applied currents. If activity occurs during MREIT imaging, increased neural activity rates should become visible as small increases in apparent conductivities of voxels coincident with active cell regions. MREIT voxels within active tissues are sensitive to these small conductivity shifts. Computer simulations have indicated (Sadleir et al., 2010) that imaging of small cell preparations may be feasible with high signal to noise ratio (SNR) levels and moderate resolutions. MREIT imaging necessarily involves application of current, which in general may change the underlying activity levels, thus making MREIT naturally suitable for studying the effects of electrical stimulation therapies or for the study of differential activity caused by application of current combined with a drug or other intervention.

In this study, we demonstrated the existence of MREIT neural activity contrasts *in vitro* using the abdominal ganglion of *Aplysia Californica*, a commonly studied neural complex (Frazier et al., 1967; Grant et al., 2000; Novak and Wheeler, 1986; Radecki et al., 2014). MREIT phase data from a test chamber containing the isolated ganglion were gathered, first, when the ganglion was spontaneously spiking in seawater background solution (PRE), and secondly in a state where increased activity was provoked by injection of a presumed excitotoxic solution (KCl-doped seawater) into the test chamber (POST). The effect of this agent was confirmed by separate microelectrode array (MEA) recordings. In a final phase of each experiment, performed approximately 19 hours after the sample was placed in the machine, the same image set was acquired from the ganglion remains (DEAD). Within each phase of each experiment, data were also gathered from ganglia with no injected current (NC), providing an opportunity to qualitatively compare findings with those in ncMRI studies (Huang, 2014; Huang and Zhu, 2015; Jiang et al., 2014; Luo et al., 2009).

We provide an overview of MREIT image parameters and factors affecting signals and contrast in Appendices A and B. Because the effect of passive tissue conductivity dominates current flow, it was only possible to confirm the contrast caused by activity by applying a treatment to modify spike rates. Experiments were performed at two different MREIT imaging current amplitudes, and matched controls were employed to further validate results. Data were analyzed in terms of absolute and relative standard deviations observed in phase data in regions of interest corresponding to the *Aplysia* tissue (AP) or background media (BK). Because MREIT sequences used were long relative to typical interspike intervals, and only spontaneous activity was studied, we did not expect any coherent association between activity location or timing. We therefore anticipated that phase changes accumulated over an entire imaging sequence would be more variable over voxels within active tissue when there was more spiking activity, than during a state with less average activity.

Since the mechanism of the MREIT image contrast is scalar, and therefore not diminished by superposition of multiple neural fields, it can be applied in large tissue samples and *in*

vivo. This study thus serves as an in vitro proof of concept exercise to confirm the viability of this predicted contrast mechanism.

2. MATERIALS AND METHODS

2.1. Animal Preparation, Controls and Treatments

Thirty small juvenile (<100 g) *Aplysia* were obtained from the National Institutes of Health/University of Miami National Resource for *Aplysia* Facility. Animals were anesthetized with $MgCl_2$ solution (77 g/L of $MgCl_2$ and 3.6 g/L of HEPES buffer) injected into the foot process, middle, and head as a paralytic, followed by a mid-dorsal, longitudinal incision to remove the abdominal ganglion, located on the posterior side of the animal near the gonopore. Following removal, the extensions of the abdominal ganglion were trimmed and the ganglion body was placed into a solution of artificial seawater (ASW).

2.2. Control and Treatment Solutions

Two solutions were used in this study. One was ASW, which was the native medium of the animals. The composition of ASW was as follows: NaCl (0.35 mol/L), $CaCl_2$ (0.011 mol/L), $MgCl_2$ (0.055 mol/L), KCl (0.010 mol/L) and HEPES (0.015 mol/L). The conductivity of this solution was calculated to be approximately 5.8 S/m at a temperature of 25 °C. ASW was used as the initial environment for ganglia in all experiments, and extra ASW was added as a control solution. A similar solution that had a larger concentration of potassium ions added was used as a treatment. This KCl-doped solution contained NaCl (0.35 mol/L), KCl (0.45 mol/L), $MgCl_2$ (0.055 mol/L), $CaCl_2$ (0.011 mol/L) and HEPES (0.015 mol/L). The approximate conductivity of this solution at 25 °C was calculated to be 6.6 S/m.

2.3. Microelectrode Array Reference Experiment

Before MREIT experiments commenced, the effect of adding treatment or control media to abdominal ganglion cells on average spiking rates was tested by administering solutions to 6 ganglion samples placed into the center of a microelectrode array (MEA) dish (MEA60-200-30-3D, Qwane, Lausanne, Switzerland). The surface of the MEA was treated with polyethyleneamine to improve tissue adhesion. The ganglia were initially placed in the center of the dish in approximately 500 μl ASW, and activity was recorded using a standard MEA amplifier system (MEA-60, MultiChannelSystems, Reutlingen, Germany). Recordings were made continuously before and after treatment with 500 μl KCl or ASW solution (added via a syringe over a period of 50 s), and continued for approximately 60 minutes. No current was applied to ganglia used in these experiments. Spike detection was performed on each recording using MEABench software (http://www.danielwagenaar.net/res/software/meabench/) at a 5σ threshold for treatment animals, and a 4σ threshold for controls.

2.4. MREIT Test Chamber

The remaining 24 ganglia were used in MREIT experiments. A custom test chamber was constructed for use in experiments. The test chamber consisted of an acrylic cylinder with an external diameter of 8 mm (internal diameter 4 mm) and a length of approximately 30 mm (Figure 1). There were four 2 mm diameter ports spaced at 90° intervals in a single plane near the base of the chamber. The ports were sealed with 1.5 mm-thick hydrogel/carbon

fiber electrodes (Hurev Co. Ltd, Republic of Korea), each having an area approximately 8 × 4 mm^2, which permitted application of current in two diametric directions.

Initially, a small amount (approximately 100 μl) of control ASW solution was injected into the test chamber minutes before the ganglion was placed inside. The ganglion was then gently pushed down onto the chamber base with a small copper tool.

2.5. MR Imaging Parameters

The modified spin-echo pulse sequence shown in Figure 2 (Scott et al., 1991) was used to acquire all MR data. Imaging was performed using an 11.75T Bruker Avance spectrometer (Bruker, Billerica, MA, USA) equipped with a Micro2.5 microimaging system. The test chamber was centered inside a 10 mm diameter linear birdcage coil for data collection. The imaging parameters were TR/TE = 330/14 ms, FOV = 8.95×8.95 mm^2, slice thickness Δz = 500 μm, number of averages NEX = 8, matrix size = 128×128 (pixel dimension 70 μm) and number of slices = 11. The total time required for each scan was 338 s.

2.6. MREIT Current Application

A custom-designed MREIT current source (Kim et al., 2011) was used to inject current via the electrodes and generate phase data. Two MREIT current amplitudes were tested: 1 mA (12 ganglia: 6 treatment and 6 control) or 100 μA amplitude (12 ganglia: 6 treatment and 6 control). Total current injection times (T_c) in all cases where current was used was 6 ms.

2.7. MREIT Experimental Sequence

Each ganglion was scanned first with no current (NC). A scan was then acquired for a diametric current injection I_{1+} using a sequence where a positive current pulse was applied after the 90 degree RF pulse, and a negative current pulse after the 180 degree refocusing pulse. A second image was then acquired using the identical current injection pattern, but with current polarities reversed (I_{1-}). Two similar scans were then acquired, using the same procedure but injecting current through the other pair of diametrically opposed ports, forming I_{2+} and I_{2-}. These NC, I_1 and I_2 images formed the PRE data set. A solution of either 100 μl of additional ASW (12 control cases: 6 1 mA and 6 100 μA) or 100 μl of KCl-doped ASW (12 treatment cases: 6 1 mA and 6 100 μA) was then added to the chamber via a syringe pump. The solution administration procedure took approximately 10 minutes, one minute of which involved adding fluid to the chamber (the fluid bolus was placed midway along an air-filled tube). This procedure was chosen to avoid the possibility that the extra fluid would dislodge the ganglion from the base of the chamber. This was followed by a delay of about 20 minutes to allow the treatment solution to take effect.

A second sequence of five scans: NC, I_{1+}, I_{1-}, I_{2+} and I_{2-} was then acquired (POST). The test chamber was held in the magnet until approximately 19 hours after PRE imaging commenced. A final scan set of the ganglion remains was then acquired (DEAD). The full imaging sequence is summarized in Table 1.

Note that experiments on each ganglion were labeled according to the MREIT current level used, and whether the control or treatment solution was administered (for example '1 mA, control') even though each experiment included NC images gathered as part of the protocol.

2.8. MREIT data preprocessing

Both magnitude and phase images were reconstructed directly from raw spin echo data using MATLAB (Natick, MA, USA). No phase unwrapping was required. MREIT I_{1+} and I_{1-} image data were complex divided (subtracted) to increase MREIT phase amplitudes by a factor of two (Sadleir et al., 2010), thus forming ϕ_1. This process was repeated with I_{2+} and I_{2-} to obtain the second MREIT data set ϕ_2. While each MREIT image was constructed from two acquisitions, only one acquisition was needed for NC data, resulting in three analyzed PRE image sets, three POST and three DEAD: 9 image sets in total for each experiment. As noted in Appendix A, the average of + and − data from sets of MREIT data, ϕ_d^{AVG}, should recover images similar to NC. However, this should only be the case overall for BK ROIs, (and DEAD images of AP ROIs) because averaged MREIT data may also include effects of activity. In Appendix C, we confirm the statistical similarity of NC and ϕ_d^{AVG} data in BK ROIs for 1 mA experiments. An alternative analysis to establish fMREIT contrasts could involve ϕ_d^{AVG}, but we do not present these results here.

Subtracted fMREIT image data were analyzed in raw (phase) form, without transformation to equivalent magnetic flux densities. This allowed for comparisons with NC data at the same scale. Factors affecting phase data with and without neural activity are considered in Sections 2.10 and 2.11 below.

2.9. Region of Interest Segmentation

One or two slices containing voxels corresponding to the ganglion body (AP) or background solution (BK) were identified manually from the 11 magnitude slices of PRE NC data for each ganglion. Portions of background slices were masked out if parts of data were unusable due to, for example, the chamber walls, injection port, or bubbles. For conditions when current was applied, only half of BK slices were used: the top half for I_2 and the left half for I_1. Illustrations of AP and BK slice choices and regions of interest (ROIs) are shown in Figure 4. Once segmented, standard deviations in phase were obtained by partitioning each slice (identified as either AP or BK) into 4×4 voxel segments in designated AP or BK slices and then calculating standard deviations in each 4×4 segment within the segmented ROI. Segments with fewer than 3 voxels were discarded, so that standard deviations were calculated from between 3 and 16 values.

2.10. Expected MREIT and NC Baseline Phase Noise Levels

Each measure, $\phi_{NC,k}$, $\phi_{d,k}$ or $\phi_{d,k}^{AVG}$, was also affected by instrument noise ε, which depends inversely on magnitude image SNR (Sadleir et al., 2005). The predicted baseline noise in subtracted phase images $\phi_{d,k}$, is (Sadleir et al., 2005)

$$\varepsilon_M^d(\phi_{\boldsymbol{d},\boldsymbol{k}}) = \frac{\sqrt{2}}{Y_M} \quad (1)$$

where $\boldsymbol{Y_M}$ is the signal to noise ratio (SNR) in magnitude images. The average SNR calculated over all experiments was used in baseline noise calculations.

Baseline noise in NC data using samples from BK compartments in DEAD ganglia were also compared with MREIT results. In the single scan NC data, the expected baseline noise was

$$\varepsilon_M^{NC}(\phi_{\boldsymbol{NC},\boldsymbol{k}}) = \frac{1}{Y_M} \quad (2)$$

because NC noise statistics did not include subtraction effects.

SNR values were calculated in this experiment by determining mean signal magnitude. Specifically, we determined an average over a portion of the magnitude image in the test chamber interior, and dividing this value by the standard deviation of a portion outside the test chamber. The result was multiplied by a factor of 0.655 to account for the difference between noise distributions inside and outside the test chamber (Sadleir et al. 2005). The scans used in determining magnitude SNR for each of the 24 ganglia experiments was the second PRE scan, i.e., I_{1+}. The slice chosen was that selected as the BK slice, as described in Section 2.9 above. The voxels used from the BK slice were a subset of those used in corresponding phase images and were chosen so that they appeared most uniform. The exterior portion was the 30 × 30 voxel corner of the image that appeared most uniform. The 24-experiment average of the individual experiment SNR values was used in calculations of (1) and (2).

2.11. Levels of Confounding Effects

Because experiments involved addition of treatment or control solution, and increasing conducting volume within the sample chamber changes current flow characteristics, we modeled effects of volume addition with reference to a finite element model (Appendix B.1). We also tested a hypothesis that addition of treatment media may also have caused changes in cell volumes, in addition to changing activity levels using a modified version of the same model (Appendix B.2).

2.12. Statistical Analysis

For the MEA reference experiment, a cumulative spike count over time curve for each channel was plotted to determine the channels that clearly revealed ganglion spiking activity. The spike count function was smoothed using kernel density smoothing. The spike rate (number of spikes per second) for each active channel over time was the kernel density smoothed numerical derivative of the cumulative spike count over time curve. The average

spike rates of active channels at different time points were estimated using linear regression on a log-transformed rate to improve the normality of the residuals.

In segmented and blocked AP or BK MREIT data, linear regression was used to estimate the average standard deviation in phase (calculated as described in section 2.9) fit by maximum likelihood estimation. A natural log transformation of the standard deviation was employed to improve the normality of residuals. A random effect was used to account for the likely correlation of values from the same ganglion, slice and condition. Models were fit for BK and AP separately because the variation in standard deviation was expected to be much greater for AP than BK. In the AP model, the PRE NC standard deviations were used to control for the activity level of the ganglion. Average MREIT standard deviations over blocks of voxels in AP and BK ROIs for each cohort (1 mA control, 1 mA treatment, 100 μA control and 100 μA treatment) were pooled into PRE, POST and DEAD phases and then analyzed.

We applied a second method to examine changes from initial activity. Relative standard deviation (RSD) was calculated by dividing POST or DEAD standard deviations by corresponding PRE standard deviations. For example, POST NC was divided by PRE NC and POST I_1 was divided by PRE I_1 data. This was done at the 4×4 block level, e.g., the standard deviation of POST NC phase for the block containing the voxel (60, 75) on slice 8 was divided by the standard deviation of the same block on the same slice at PRE NC. Linear regression modeling was used again to estimate average RSD, where, again, log-transformation was necessary.

Statistical analysis was carried out in Stata MP Version 13.2 (Lakeway Drive College Station TX). Significance was determined at the 5% level.

2.13. Data Analyzed

In MREIT experiments, data were planned to be collected from 24 ganglia in each of the nine different conditions shown in Table 1. However, data were not acquired for some ganglia in some conditions due to some lack of adherence to protocol. For example, some images were acquired using 16 averages rather than eight, so these images were discarded. This affected four ganglia in the treatment group at 100 μA. In 100 μA control ganglia, (Aplysia 30–35) no timing information for DEAD images was recorded; thus these conditions were not analyzed for this group. Full details of experimental settings are in Table 2. Bubbles were occasionally visible in phase and magnitude data, usually in the BK slice, so for some samples only part of the BK slice could be used.

In total, data were analyzed from 49 slices from 24 ganglia, giving 202,298 ϕ measurements. Partitioning into 4×4 contiguous blocked segments produced 16,140 standard deviations, of which 11,954 were BK and 4,186 were AP.

3. RESULTS

3.1. MEA Results

Results of MEA monitoring are summarized in Figure 3. In Figure 3, average spiking rates for the three treatment and three control animals are shown with 95% confidence intervals (CI). Spiking rates of treatment animals varied post treatment administration, but were significantly increased above initial levels after around 30 minutes (AP A N=3636, $p<0.001$, AP B N=4944, $p<0.001$, AP C N=3346 $p<0.001$), corresponding to the times at which time POST MREIT images were acquired during imaging. One of the treatment ganglia (AP A) was more active than the other two and spike rates for this sample are plotted on a different scale (maximum at 3 Hz). Spike rates for the three control animals were overall lower than for treatment animals. Spike rates in all three control animals were not significantly different than their initial values at 30 minutes after media addition (AP D N=3475 $p=0.975$, AP E N=3477 $p=0.555$, AP F N=3849 $p=0.807$). However, all control tissue spiking rates appeared to decrease towards the end of monitoring periods. We believe that similar responses were followed by ganglia in MREIT studies, so that POST treatment images were acquired when activity was likely to be elevated relative to PRE states, and that control ganglion POST images were representative of similar or lesser activity relative to PRE states.

3.2. Raw Image Data

Figure 4 shows example regions of interest (ROIs) and phase data for Aplysia 18 (1 mA, CONTROL) Phase changes within the AP ROI for current direction I_1 (Figure 4 A) were of the order of 0.02 rad (minimum -0.22, maximum 0.21 rad). Example magnitude (top) and phase (bottom) images for I_1 and I_2 MREIT current flow at 1 mA amplitude are shown for the BK slice for this ganglion in Figure 4 (C and D). Phase ranges over BK ROIs were of the order of 0.16 rad (minimum -0.04, maximum 0.12 rad). Current flow in Figure 4 (C) was from left to right, as is clear from the distribution having negative values (darker) in the lower half of the image and brighter values above the midline. In Figure 4 (D) current flow was from bottom to top of the image because negative values were on the right-hand side of the phase image. Also shown in Figure 4 are NC data for the BK ROI (Figure 4 B). We found that NC and MREIT phase images appeared as expected. Figure 5 shows examples of 4 × 4 block segments described in Section 2.9 for (A) Aplysia 18 (control) for ϕ_1, ϕ_2 and NC conditions and (B) for Aplysia 12 (treatment) ganglia at 1 mA. The BK blocks shown in Figure 5A illustrate, respectively, 108 of the 578 NC voxels, 61 of the 359 I_1, and 61 of the 338 I_2 4 × 4 BK blocks used in the linear regression model described in Section 2.10. Total counts for the 1 mA control condition are also shown in Tables 3 and 4. Similarly, the AP blocks in Figure 5A (top) show that data from this experiment contributed 28 of the 164 4×4 AP blocks analyzed for this condition.

Note that in both Figures 4 and 5, the variability in the AP ROI was high for both PRE and POST segments, but less so for DEAD. This was because the major effect on passage of current through the tissue was its conductivity distribution. With intact cells (PRE and POST) the current flow was dominated by the tissue structure, and in DEAD tissue cell walls had broken down, leading to a more homogeneous conductivity distribution.

3.3. MREIT Baseline Noise Levels

The average signal to noise ratio (SNR) $\boldsymbol{Y}_m$ was estimated to be 113.2 (n=24, [106.1, 120.2] 95% CI) from the 24 128 × 128 resolution magnitude images. Substituting this into (1) predicted baseline noise levels in subtracted data of 0.0125 rad ([0.0133, 0.0118] 95% CI), or 0.716° ([0.76, 0.67] 95% CI). This established the MREIT noise floor ε_M^d for the experiment.

Baseline noise levels predicted in the single scan NC data sets, ε_M^{NC}, were predicted to be, via (2), 0.0088 rad ([0.0094, 0.0083] 95% CI). Actual standard deviations in BK PRE NC data, which would have been affected by systematic phase artifacts, were larger than these estimates, averaging 0.0098 rad (n=1,969, [0.0092,0.0103] 95% CI), or 0.56° ([0.53,0.59] 95% CI).

3.4. Dilution and Cell Size Effects

Results of tests to determine extents of media dilution and changes in cell size are summarized in Appendix B.1 and B.2 respectively. We found that addition of control media should have produced decrease in B_z signal scale of around 20%, and addition of treatment would have produced a decrease of around 24%. Cell diameter decreases of 2.5% changed B_z standard deviations in an ROI covering nine simulated cells by at most 0.64%.

3.5. MREIT Phase Standard Deviation by Current Direction

The remainder of our analysis describes the results obtained using random effect linear regression modelling. First, we sought to confirm that the direction of the current did not have a significant effect on phase standard deviation. To this end a model was fit to the log-transformed BK phase data with current, where we estimated average phase standard deviation for each treatment/current group by condition. There was a total of 24 groups and therefore averages employed in the study, comprising, the eight treatment/current/direction combinations (2^3) and the three experimental segments (PRE, POST and DEAD). Only 22 averages, which were two short of 24 since there were no usable data for DEAD control 100 μA, were used in analysis. A Wald test for equality of the 11 pairs that differed only by the direction of their current resulted in a p-value of p=0.9978, indicating no significant effect of current direction for BK. A similar model was applied to AP data and resulted in a p-value of p=0.9796. Therefore, for the remainder of the analysis, the data from I_1 and I_2 current directions ($\boldsymbol{\phi}_1$ and $\boldsymbol{\phi}_2$) were pooled.

3.6. MREIT Phase Standard Deviation Analysis

We now describe the results shown in Figure 6. Table 3 shows the corresponding counts and medians of phase standard deviations for both BK and AP ROIs by condition. These are average standard deviations estimated using a linear regression of the natural log of the standard deviation of phase data multiplied by 100. The PRE NC data for AP were estimated separately so that their initial values could be used to control for ganglion activity level (n=501, standard deviation in residuals σ_e=0.0057 rad, shown in Figure 6 D). Doing so in the model on AP data from conditions other than PRE NC revealed a significant effect of

initial activity level (p-value<0.001). The averages were predicted at the average initial activity level of all ganglia (n=3,685, σ_e=0.0042 rad, shown in Figure 6 B and D).

For BK data, two separate models were fit, with current (n=6,578, σ_e=0.0035 rad) and without current (n=5,376, σ_e=0.0033 rad), again because the variation was expected to be different (shown in Figure 6 A and C). While these two variations appeared close, they were significantly different at the 95% confidence level: [0.003452, 0.003573] with current and [0.003220, 0.003344] without current.

We expected that estimates of baseline phase noise calculated using (1) would be less than the standard deviations found in BK data, because BK data included the background magnetic flux density distribution. Plots of baseline noise confidence intervals for both MREIT and NC data are shown overlaid on Figure 6. Estimates from (1) were overall slightly lower than observed standard deviations in BK data. Standard deviations found in PRE BK data for 1 mA data were significantly higher (0.0141 rad ([0.0132, 0.0149] 95% CI)) than for corresponding 100 μA data (0.0115 rad ([0.0108, 0.0122] 95% CI)), p<0.001 (n=2,797). However, because the signal component in BK compartments contributed from the magnetic flux density distribution was small in comparison with ε_M^d, and because different ROIs and therefore field geometries were compared in each experiment, there was no simple tenfold increase in standard deviations between experiments performed at the two current levels.

Of most interest was the comparison of PRE to POST for AP (Figure 6 B). The p-value of the test comparing average standard deviation for treatment AP with 100μA (light blue) PRE-MREIT to POST-MREIT was p=0.048. The p-value of the test comparing average standard deviation for treatment AP with 1mA current (dark blue) PRE-MREIT to POST-MREIT was p=0.001. The p-value of the test comparing average standard deviation for control AP with 100μA (orange) PRE-MREIT to POST-MREIT was p=0.273. The p-value of the test comparing average standard deviation for control AP with 1mA current (red) PRE-MREIT to POST-MREIT was p=0.001 (seen as decreasing). We could not do any test comparing PRE-NC to POST-NC since the PRE-NC was used as an explanatory variable in the AP model.

In summary, we found a significant increase in phase standard deviation due to the treatment and 100 μA current, with a more significant increase when the current was 1mA. Standard deviations in BK data at different current levels increased significantly with current amplitude, as expected.

3.7. MREIT Phase RSD Analysis

We now describe the results shown in Figure 7. These are average RSDs estimated using two linear regression models (n= 7,034 for BK and n=2,487 for AP). Of most interest is the comparison of POST to 1 (an RSD =1 meant no change) for AP (Figure 7 B). The p-value of the test comparing average RSD for treatment AP and 100μA (light blue) POST-MREIT to 1 was p=0.1121. The p-value of the test comparing average RSD for treatment AP and 1mA current (dark blue) POST-MREIT to 1 was p=0.0016. The p-value of the test comparing average RSD for control AP and 100μA (orange) POST-MREIT to 1 was p=0.2017. The p-

value of the test comparing average RSD for control AP and 1mA current (red) POST-MREIT to 1 was $p<0.001$ (decreasing). In summary, we found a significant increase in phase RSD due to the treatment when the current was 1mA (1 mA effect size d=2.76). The observed control effect size at 1 mA was d=-7.1. Table 4 shows corresponding counts and medians of relative RSDs for both BK and AP by condition.

4. DISCUSSION

4.1. Anticipated Findings

Intrinsic neural currents should produce dipole like biases on phase data (Konn et al., 2003). This should also be the case in MREIT data influenced by both neural currents and conductivity changes (Sadleir et al., 2016). Therefore, in these experiments we sought only to image the effect of overall increases in spiking activity on phase variability.

Although spontaneous activity in the ganglion model was not predictably located in time or space, our experiment was able to determine if MREIT could distinguish between lower time- and space-averaged levels of activity, or higher ones caused by treatment administration. We expected that an increase in activity would be indicated by an increase in standard deviations of AP voxels (Song et al., 2016a).

We believed that this experiment could distinguish the difference between the different activity levels and their resulting influence because a) the exact same regions of interest were compared in three states, PRE, POST and DEAD; b) we were able to compare NC and two imaging amplitudes of MREIT data for the same ganglia and c) comparison of two regions of interest, AP and BK within each data set was also performed.

4.2. Main Findings

The main finding relating to the existence of the MREIT contrast mechanism is shown in Figure 7 (B) where only AP compartments of treated ganglia showed a significant increase in variability PRE to POST. The observed effect was significant at higher current. In control ganglia, no significant increase was observed. No significant change was observed in the identical compartments of NC images for each experiment, as shown in Figure 7 (D).

In both MREIT and NC cases there were significant decreases in standard deviations between DEAD and PRE cases of AP ROIs, which would be expected principally because tissue disintegration resulted in more homogeneous conductivity distributions.

Changes in BK compartments were not significantly affected by treatment or control and were similar in PRE, POST and DEAD cases for both MREIT and NC images. Observation of stable BK data confirmed that the differences observed in AP compartments were actually caused by changes in tissue properties, and not by other factors created during imaging.

In the sections below we describe findings comparing noise levels in BK and AP compartments for experimental conditions with and without current, and before and after administration of control or treatment solutions. We compare these findings in detail with expectations.

4.3. Baseline Noise Levels in MREIT Images

Baseline phase noise levels in MREIT data were observed to be in the range of 0.0062 rad (1), which was approximately half the standard deviation found in PRE BK data. In DEAD, BK NC data we found standard deviations in phase data of around 0.0096 rad. Baseline noise levels were found to be similar in all MREIT data for all ganglion experiments at both current levels, and regardless of whether treatment or control solution was used.

4.4. Dilution Effects

Inspection of sagittal images of the test chamber PRE and POST fluid administration revealed that most fluid was added far above the electrode plane. We estimated the expected decrease by referring to computational models constructed from magnitude images of the test chamber before and after solution addition. Only small (20% for control and 24% for treatment) decreases in signal amplitudes were predicted by models (Appendix B.2). In most BK MREIT data (Figure 7 A) we observed a slight decrease in RSD (although values were not significantly different from 1). We conclude this was most likely caused by dilution effects.

4.5. Changes in BK – Expectations and Findings

As MREIT imaging current increased, we also expected to see an increase in standard deviations of all voxel samples because of the increased phase distribution bias it caused (Figure 4). This was expected to be most easily observed in BK ROIs.

Figure 6 (A) and Table 3 both show that although standard deviations were larger in both 1 mA MREIT cases than both 100 μA cases, the standard deviations for the 1 mA cases were only about 50% higher than at 100 μA. This was most likely because the influence of baseline noise level ε_M^d on the phase data was large relative to the phase standard deviations caused by imaging current flow.

Standard deviations in BK compartments were not significantly different between PRE, POST and DEAD states for each current level. POST and DEAD standard deviations were generally lower than in PRE cases because of dilution effects.

Since BK compartment findings agreed with expectations across multiple experiments and current levels, this increased our confidence in findings from AP compartments. Observations in AP compartments are discussed below.

4.6. Changes in AP – Expectations and Findings

We would expect for control ganglia, where activity levels were assumed to be the same for PRE and POST segments, that POST standard deviations in the AP compartment would be similar or slightly lower than those found PRE due to dilution effects. In treatment ganglia, POST standard deviations would be expected to be larger than PRE. We expected the MREIT current amplitude effect observed in BK ROIs would not have been observable in AP compartments because of the larger influences of individual tissue heterogeneity and activity levels.

Overall, there were clear differences between control and treatment conditions for POST MREIT images, shown in relative terms in Figure 7 (B) and Table 4, or by inspecting individual PRE to POST changes shown in Figure 6 (B) and Table 3. There was no significant increase in standard deviations in control ganglia PRE to POST, but significant increases for treatment animals at 1 mA and 100 μA (Figure 6). The p-values found for 100 μA were lower than for 1 mA, which supports the argument that the size of the MREIT contrast should depend on current amplitude (Sadleir et al., 2010). Significant decreases were observed in absolute and RSDs of 1 mA POST control data relative to PRE cases ($p<0.001$). Control ganglia were observed in reference MEA data to decrease activity levels over time, but not significantly (Figure 3). We speculate that the significant decreases in absolute and relative control standard deviations at 1 mA may have been related to changes in spiking rates over time, this time decreasing. The decrease observed in controls at 100 μA was not significant ($p=0.273$), further indicating a current amplitude effect.

For 1 mA, control ganglia showed significantly larger standard deviations PRE than any of the other three groups. These same animals showed a large standard deviation decrease in POST imaging. Note that it is not possible to directly relate isolated standard deviations to activity levels in isolation (Appendix A). However, it was not clear why standard deviations in PRE experimental segments at this current level were larger than in the other experimental groups. It may have been because the MREIT current source settings changed between the two sets of experiments due to the following factors: different animal stocks used, different preparations of solution batches, combined with the sequential nature of the experiment (Table 2).

In NC data from AP slices (Figures 6 and 7 D), there was no significant difference between PRE and POST average standard deviations for all ganglion groups. Standard deviations in PRE and POST NC data were of the same order as the highest values found for MREIT cases (Figure 6 B and D). However, MREIT and NC images had different noise characteristics and constructions (Appendix A). In NC data, while we found large standard deviations for all ganglia in PRE and POST phases there was no significant difference between these two conditions, which we believe was because any neural current related effects in NC AP data were smaller than the baseline phase noise levels. We believe that standard deviations in all NC AP data were only representative of static phase artifacts in Aplysia ROIs, with standard deviations in the NC AP ROIs being higher than corresponding BK ROIs because of tissue inhomogeneity (Appendix A).

4.7. DEAD Conditions — Expectations and Findings

For MREIT data, POST and DEAD NC standard deviations were statistically similar in the BK compartment (Figure 6 A), but those in the AP compartment were found to be much smaller for DEAD cases than in PRE cases (Figures 6 and 7 B). All standard deviations were statistically similar for both treatment and control AP compartments in DEAD conditions. RSDs in the AP compartment for all DEAD/PRE comparisons were less than one for all ganglia and for all currents. This was primarily because tissue disintegration decreased the AP ROI heterogeneity.

We found that in POST and DEAD NC images (Figure 6 C) there was no significant change in BK compartments, but there was a large decrease in standard deviations in AP compartments for DEAD relative to PRE measurements. Again, it is most likely that this was caused by tissue disintegration.

4.8. Experimental Limitations

In nearly all cases in this study, ganglia were put into treatment or control groups sequentially (Table 2). This could have led to differences associated with, for example, animal batch, changes in current source calibration, or formulation of ASW or KCl-doped solution. However, the experiment was planned this way as randomization of treatment and current would have increased protocol complexity, and thereby impacted protocol adherence.

4.9. Comparison with Other MR-based Measurements of Neural Activity

While no previous experiments on MREIT detection of neural activity have been published, there are several published experimental ncMRI studies (Huang, 2014; Huang and Zhu, 2015; Jiang et al., 2014; Luo et al., 2009; Park et al., 2006; Petridou et al., 2006). Petridou et al. (Petridou et al., 2006) reported significant differences in spectroscopic images caused by administration of TTX to cultured tissue. However, most studies have reported no significant differences in images related to activity level. Although none of the previous ncMRI studies used conditions similar to our experiment, we can at least categorize our findings relative to this literature by comparing NC findings. Because we found no significant changes PRE to POST in NC data, this finding supports modeling and experimental studies that suggest that phase changes caused by neural currents alone may have been too small to be detected above the noise floor (Cassarà et al., 2008; Hagberg et al., 2008; Hagberg et al., 2006; Konn et al., 2003).

4.10. Implications for Future Experimentation

4.10.1. Temporal Resolution and Imaging Strategy—In this study, we used conventional spin echo-based MREIT images, rather than a faster echo planar imaging (EPI) sequence. This was done for comparison with existing MREIT literature. In a conventional spin echo sequence sampling random activity, for each line of k-space acquired, a different, random assay of activity is measured. This will be compounded when phase images collected with different current polarities are averaged, and finally subtracted to form an MREIT image. Thus, in these experiments, by using 128 phase encoding steps and 8 averages there were at least 1024 separate samples of spontaneous activity collected in each image. Data collected this way during each stage of I_1, say, I_{1+}, was then subtracted from another set of 1024 samples to form I_{1-}. Therefore, we believe that MREIT phase images should have been, on average, sensitive to differential apparent conductivities in active cells caused by the treatment, but because of the method of acquisition and the averaging strategy no detailed temporal information would have been discernable.

As this first test, measurement of neural activity using MREIT was successful because we did observe differences between control and treatment groups using this strategy, and the increase in activity caused by KCl was confirmed by MEA experiments. However, it would be desirable to increase the temporal resolution of images. In future experiments, we plan to

use EPI sequences (Chauhan et al., 2017) combined with undersampling (Song et al., 2016b) to assess activity at speeds similar to BOLD fMRI.

4.10.2. Analysis of Spontaneous Activity—Analysis of these data was only possible using standard deviations in data acquired over relatively large periods of time, and over relatively large spatial ROIs. Again, this was done because of limitations arising from the spontaneous nature of the activity in the experiment. A more precise temporal and spatial investigation into the mechanisms responsible for our observed contrast would be possible if evoked responses were generated and locked to imaging sequences.

4.10.3. Verification Against Independent Activity Analyses—In this study, we were not able to contemporaneously monitor activity using a reference method because of limitations of the MEA recording system. Results shown in Figure 3 were gathered on other ganglion samples. While the media concentrations and dilution factors were the same in MEA and MREIT recordings, different volumes were used, because of the different chamber volumes, and is possible the activity recorded may not have been the same as in MREIT experimental tissue. MEA recordings showed on average larger variability in treatment cases compared to controls, but responses and response variability may have been different in both treatment and control cases for two reasons. First, MEA recordings were made from animals not exposed to imaging currents; and it is not clear exactly how this exposure may have affected activity levels afterwards. Current administration may conceivably have sensitized tissue and changed the activity levels. However, MEA recordings we have made interleaved with administration of MREIT-like current following addition of (different) treatment or control solutions have not shown effects different from treatment or control administration alone. Finally, it is indeed possible that co-administration of control or treatment solutions and MREIT imaging currents caused different levels of activity than shown in Figure 3. Such an effect of imaging current on activity level is likely and may be useful in exploring effects of neuromodulation (Sadleir et al., 2010). It is difficult to demodulate spike recordings from MREIT imaging currents to explore this in MEA data directly (Elmariah et al., 2006). In recent experiments, we have incorporated MEA electrodes into the base of a test chamber placed into the bore of the imaging system. While simultaneous imaging and MEA monitoring is not possible, we will therefore be able to interleave MEA and MREIT measurements in order to verify activity levels on a per animal basis.

4.10.4. In vivo MREIT Imaging Implications—In vivo imaging has been tested in MREIT in some studies, for example (Kim et al., 2009) but no in vivo fMREIT studies have yet been tried. One advantage that fMREIT may have over ncMRI is that it may be possible to detect activity in complex neural architecture because contrast is controlled by a scalar rather than vector parameter. However, one critical in vivo factor that may affect the conductivity contrast mechanism is the presence of blood flow. Blood conductivity is relatively large, around 0.67 S/m (Geddes and Baker, 1967) and blood flow changes or associated BOLD effects caused by activity could potentially affect signals caused by membrane conductance conductivity changes. The extent of these effects would depend on the spatial and temporal resolution of scans since fast scanning, or scanning after blood flow has reached steady state (Bandettini et al., 2005), may allow these influences to be separated.

5. CONCLUSIONS

We performed an experiment designed to confirm the presence of an activity-related effect on MREIT data using a spontaneous activity model. Analysis of spatially and temporally averaged MREIT phase images showed significant increases between standard deviations within active tissue when an excitotoxic doped treatment was applied, versus a control solution. No significant difference was found in similar images acquired with the same imaging strategy, but no imaging current. Images gathered at two different current amplitudes showed similar and significant differences between standard deviations measured in treatment and control states.

We conclude that these results strongly suggest that the measured contrasts in MREIT data were due to different spiking levels, and that functional MREIT (fMREIT) has promise as a direct method of imaging neural activity.

Acknowledgments

This work was supported by the National High Magnetic Field Laboratory and the National Institute of Neurological Disorders and Stroke of the National Institutes of Health under Award Number R01NS077004 (RJS). RJS thanks Dr Tom DeMarse (University of Florida) for his assistance with MEA recordings.

ABBREVIATIONS

MREIT	Magnetic Resonance Electrical Impedance Tomography
fMREIT	functional MREIT
ASW	Artificial Seawater
ncMRI	neural current MRI
SNR	Signal to noise ratio
ROI	Region of interest
EPI	Echo planar imaging
NC	Image gathered with no imaging current
MREIT	Image gathered using either 100 μA or 1 mA imaging current
PRE	Image acquired before addition of KCl solution
POST	Image acquired approximately 30 minutes after addition of KCl solution
DEAD	Image acquired approximately 19 hours after experiment initiated
AP	Region of interest identified containing ganglion tissue
BK	Region of interest containing background media
RSD	Relative standard deviation

References

Aristovich KY, Packham BC, Koo H, dos Santos GS, McEvoy A, Holder D. Imaging fast elecrical activity in the brain with electrical impedance tomography. NeuroImage. 2016; 124:204–213. [PubMed: 26348559]

Bandettini PA, Petridou N, Bodurka J. Direct detection of neuronal activity with MRI: Fantasy, possibility, or reality? Applied Magnetic Resonance. 2005; 29:65–88.

Bernstein, MA., King, KF., Zhou, XJ. Handbook of MRI Pulse Sequences. Elsevier Academic Press; 2004.

Cassarà AM, Hagberg GE, Bianciardi M, Migliore M, Maraviglia B. Realistic simulations of neuronal activity: A contribution to the debate on direct detection of neuronal currents by MRI. NeuroImage. 2008; 39:87–106. [PubMed: 17936018]

Chauhan M, Vidya Shankar R, Ashok Kumar N, Kodibagkar V, Sadleir RJ. Multi-shot echo-planar MREIT for fast imaging of conductivity, curent density and electric field distributions. Magnetic Resonance in Medicine. 2017 In press.

Cornbleet PJ, Gochman N. Incorrect least-squares regression coefficients in method-comparison analysis. Clinical Chemistry. 1979; 25:432–438. [PubMed: 262186]

Elmariah, H., Dockendorf, K., Zhang, S., Sadleir, RJBDT. Impedance Tomography of Aplysia Abdominal Ganglion using Multichannel Micro-electrode Arrays. Third Cairo International Biomedical Engineering Conference (CIBEC'06); Cairo, Egypt. 2006.

El-Sharkawy AM, Schär M, Bottomley PA, Atalar E. Monitoring and correcting spatio-temporal variations of the MR scanner's static magnetic field. Magnetic resonance materials in Physics, Biology and Medicine. 2006; 19:223–236.

Frazier WT, Kandel ER, Kupfermann I, Waziri R, Coggeshall RE. Morphological and functional properties of identified neurons in the abdominal ganglion of aplysia californica. Journal of Neurophysiology. 1967; 30:1288–1351.

Geddes L, Baker LE. The specific resistance of biological materials: a compendium of data for the biomedical engineer and physiologist. Medical & Biological Engineering and Computing. 1967; 5:271–293.

Grant SC, Aiken NR, Plant HD, Gibbs S, Mareci TH, Webb AG, Blackband SJ. NMR spectroscopy of single neurons. Magnetic Resonance in Medicine. 2000; 44:19–22. [PubMed: 10893516]

Hagberg GE, Bianciardi M, Brainovich V, Cassara AM, Maraviglia B. The effect of physiological noise in phase functional magnetic resonance imaging: from blood oxygen level-dependent effects to direct detection of neuronal currents. Magnetic Resonance Imaging. 2008; 26:1026–1040. [PubMed: 18479875]

Hagberg GE, Bianciardi M, Maraviglia B. Challenges for detection of neuronal currents by MRI. Magnetic Resonance Imaging. 2006; 24:483–493. [PubMed: 16677955]

Huang J. Detecting neuronal currents with MRI: A human study. Magnetic Resonance in Medicine. 2014; 71:756–762. [PubMed: 23475847]

Huang J, Zhu DC. Exploring Human Brain Neuronal Currents with Phase MRI. International Journal of Imaging Systems and Technology. 2015; 25:172–178.

Jiang X, Lu H, Shigeno S, Tan LH, Yang Y, Ragsdale CW, Gao JH. Octopus visual system: a functional MRI model for detecting neuronal electric currents without a blood-oxygen-level dependent confound. Magnetic Resonance in Medicine. 2014; 72:1311–1319. [PubMed: 24301336]

Kelly GE. The influence function in the errors in variables problem. The Annals of Statistics. 1984; 12:87–100.

Kim HJ, Kim YT, Minhas A, Jeong WC, JWE. In vivo high-resolution conductivity imaging of the human leg using MREIT: the first human experiment. IEEE Transactions on Medical Imaging. 2009; 28:1681–1687. [PubMed: 19369151]

Kim YT, Yoo PJ, Oh TI, JWE. Magnetic flux density measurement in magnetic resonance electrical impedance tomography using a low-noise current source. Measurement Science and Technology. 2011; 22:105803.

Konn D, Gowland P, Bowtell R. MRI detection of weak magnetic fields due to an extended current dipole in a conducting sphere, a model for direct detection of neuronal currrents in the brain. Magnetic Resonance in Medicine. 2003; 50:40–49. [PubMed: 12815677]

Luo Q, Gao JH. Neuronal Current MRI without BOLD Contamination. NeuroImage. 2009; 47:S39–S41.

Luo Q, Lu H, Lu H, Senseman D, Worsley K, Yang Y, Gao JH. Physiologically evoked neuronal current MRI in a bloodless turtle brain: detectable or not? NeuroImage. 2009; 47:1268–1276. [PubMed: 19539040]

Minhas A, Kim HH, Meng ZJ, Kim YT, Kim HJ, Woo EJ. Three-dimensional MREIT Simulator of Static Bioelectromagnetism and MRI. Biomedical Engineering Letters. 2011; 1:129–136.

Novak JL, Wheeler BC. Recording from the Aplysia abdominal ganglion with a planar microelectrode array. IEEE Transactions on Biomedical Engineering BME-33. 1986:196–202.

Park TS, Lee SY, Park JH, Cho MH, Lee SY. Observation of the fast response of a magnetic resonance signal to neuronal activity: a snail ganglia study. Physiological Measurement. 2006; 27:181–1990. [PubMed: 16400204]

Petridou N, Plenz D, Silva AC, Loew M, Bodurka J, Bandettini PA. Direct magnetic resonance detection of neuronal electrical activity. Proceedings of the National Academy of Science USA. 2006; 103:16015–16020.

Pourtaheri N, Truong TK, Henriquez CS. Electromagnetohydrodynamic modeling of Lorentz effect imaging. Journal of Magnetic Resonance. 2013; 236:1–9. [PubMed: 24018100]

Radecki G, Nargeot R, Jelescu IO, Le Bihan D, Ciobanu L. Functional magnetic resonance microscopy at single-cell resolution in Aplysia californica. Proceedings of the National Academy of Science USA. 2014; 111:8667–8672.

Sadleir RJ, Fu F, Chauhan M. Functional Magnetic Resonance Electrical Impedance Tomography (fMREIT) Sensitivity Analysis Using An Active Bidomain Finite Element Model Of Neural Tissue. Magnetic Resonance in Medicine Under Revision. 2016

Sadleir RJ, Grant S, Zhang SU, Lee BI, Pyo HC, Oh SH, Park C, Woo EJ, Lee SY, Kwon O, Seo JK. Noise analysis in magnetic resonance electrical impedance tomography at 3 and 11T field strengths. Physiological Measurement. 2005; 26:875–884. [PubMed: 16088075]

Sadleir RJ, Grant SC, Woo EJ. Can high-field MREIT be used to directly detect neural activity? Theoretical Considerations. NeuroImage. 2010; 52:205–216. [PubMed: 20382240]

Scott GC, Joy MLG, Armstrong RL, Henkelman RM. Measurement of nonuniform current density by magnetic resonance. IEEE Transactions on Medical Imaging. 1991; 10:362–374. [PubMed: 18222838]

Seo JK, Woo EJ. Electrical tissue property imaging at low frequency using MREIT. IEEE Transactions on Biomedical Engineering. 2014; 61:1390–1399. [PubMed: 24759274]

Seo JK, Yoon JR, Woo EJ, Kwon O. Reconstruction of conductivity and current density images using only one component of magnetic field measurements. IEEE Transactions on Biomedical Engineering. 2003; 50:1121–1124. [PubMed: 12943280]

Song Y, Jeong WCJ, WE, Seo JK. A method for MREIT-based source imaging: simulation studies. Phys Med Biol. 2016a; 61:5706–5723. [PubMed: 27401235]

Song Y, Seo JK, Chauhan M, Ashok Kumar N, Sadleir RJ. Fast, adaptive acquisition strategies for low-frequency conductivity imaging using MREIT. IEEE Transactions on Biomedical Engineering. 2016b under review.

Sundaram P, Nummenmaa A, Wells W, Orbach D, Orringer D, Mulkern R, Okada Y. Direct neural current imaging in an intact cerebellum with magnetic resonance imaging. NeuroImage. 2016; 132:477–490. [PubMed: 26899788]

Truong TK, Avram A, Song AW. Lorentz effect imaging of ionic currents in solution. Journal of Magnetic Resonance. 2008; 191:93–99. [PubMed: 18180187]

Vongerichten AN, dos Santos GS, Aristovich KY, Avery J, McEvoy A, Walker M, Holder D. Characterisation and imaging of cortical impedance changes during interictal and ictal activity in the anaesthetised rat. NeuroImage. 2016; 124:813–823. [PubMed: 26375207]

Woo EJ, Seo JK. Magnetic resonance electrical impedance tomography (MREIT) for high-resolution conductivity imaging. Physiological Measurement. 2008; 29:R1–R26. [PubMed: 18799834]

APPENDIX A Definitions and Dependences of Phase Image Data

The current density distribution caused by MREIT imaging current is related to measured magnetic flux density by Ampere's Law

$$\boldsymbol{J}=\frac{1}{\mu_0}\nabla\times\boldsymbol{B}. \quad \text{(A.1)}$$

More specifically, if there is no or little current flow out of the plane we have

$$\boldsymbol{J}\approx(J_x,J_y,0)=\left(\frac{\partial B_z}{\partial y},\frac{-\partial B_z}{\partial x},0\right) \quad \text{(A.2)}$$

This current density depends in turn on the conductivity and electric field distributions within the chamber. Conductivity distributions within the chamber $\sigma(x, y, z)$, including any heterogeneous tissue regions, will dominate current flow characteristics and therefore magnetic flux density distributions. Conductivity characteristics may in general depend on time, thus

$$\boldsymbol{J}=-\sigma(x,y,z,t)\nabla V(x,y,z). \quad \text{(A.3)}$$

The phase contribution in MR images due to externally applied currents, $\gamma T_c B_z$ (Sadleir et al., 2005), therefore depends on sample chamber shape, location of current application ports and the internal conductivity distribution, that is

$$B_z=B_z(x,y,z,\sigma(t)). \quad \text{(A.4)}$$

Consider transverse (*xy* plane) phase images with or without current, recovered from a sample chamber containing live tissue in experimental segment k = *PRE*, *POST* or *DEAD*.

From Table 1, we observe that within each segment, images were acquired for *NC*, *1+*, *1−*, *2+* and *2−*, sampling properties within the chamber over an approximate 27-minute period. For NC, we measure

$$\phi_{NC,k}(x,y,t_{NC,k})=\delta(x,y,t_{NC,k}) \quad \text{(A.5)}$$

When current is applied in direction d = 1, 2, we measure

$$\phi^{+}_{d,k}(x,y,t_{d^+,k})=\delta(x,y,t_{d^+,k})+\gamma T_c B_z(x,y,t_{d^+,k}) \quad \text{(A.6)}$$

For current where positive pulses are applied first, and

$$\phi^{-}_{d,k}(x,y,t_{d^-,k})=\delta(x,y,t_{d^-,k})-\gamma T_c B_z(x,y,t_{d^-,k}) \quad \text{(A.7)}$$

when negative pulses are applied first. Here $\delta(x, y, t_{d\pm,k})$ or $\delta(x, y, t_{NC,k})$ are the systematic phase artifacts in the image. These systematic artifact images may be inhomogeneous, for example due to imperfect shimming or susceptibility artifacts (Bernstein et al., 2004). Their overall values may also drift over time due to changes in main magnetic field (El-Sharkawy et al., 2006).

If we assume that both systematic phase artifacts δ and conductivity distributions σ are static over time, we have

$$\begin{aligned}\phi_d(x,y,t_{d\pm,k}) &= \phi^{+}_{d,k}(x,y,t_{d^+,k})-\phi^{-}_{d,k}(x,y,t_{d^-,k})\\ &= \delta(x,y,t_{d^+,k})-\delta(x,y,t_{d^-,k})+\gamma T_c\left[B_z(x,y,t_{d^+,k})+B_z(x,y,t_{d^-,k})\right]\\ &= 2\gamma T_c B_z(x,y,t_{d\pm,k})\end{aligned} \quad \text{(A.8)}$$

Similarly, under static assumptions the *average* of $\phi^{+}_{d,k}$ and $\phi^{-}_{d,k}$ will be

$$\begin{aligned}&\phi^{AVG}_{d,k}(x,y,t_{d\pm,k})\\ &=\frac{\phi^{+}_{d,k}(x,y,t_{d^+,k})+\phi^{-}_{d,k}(x,y,t_{d^-,k})}{2}\\ &=\frac{\delta(x,y,t_{1^+,k})+\delta(x,y,t_{1^-,k})}{2}\\ &=\delta(x,y,t_{d\pm,k})\end{aligned} \quad \text{(A.9)}$$

$$\text{and } \phi^{AVG}_{d,k}(x,y,t_{d\pm,k})=\delta(x,y,t_{NC,k}). \quad \text{(A.10)}$$

If there is neural activity within the sample chamber, then we assume there will be phase changes caused by magnetic fields from intrinsic sources (Konn et al., 2003). We consider these effects, which may be small, appear in in δ.

We now discuss effects on passage of MREIT imaging currents caused by membrane conductance changes in active cells. Increases in membrane conductance in active cells will allow penetration of imaging currents into intracellular spaces, effectively increasing their

apparent conductivity. Since in this case $B_z = B_z(x, y, \sigma(t))$, we cannot assume terms in $\phi_{d,k}$ or $\phi_{d,k}^{AVG}$ will cancel. We therefore must write

$$\phi_{d,k}(x,y,t_{d^{\pm},k}) = \delta(x,y,t_{d^{+},k}) - \delta(x,y,t_{d^{+},k}) + \gamma T_c\,[B_z(x,y,t_{d^{+},k}) + B_z(x,y,t_{d^{-},k})] \quad \text{(A.11)}$$

and

$$\phi_{d,k}^{AVG}(x,y,t_{d^{\pm},k}) = \frac{\delta(x,y,t_{d^{+},k}) + \delta(x,y,t_{d^{-},k}) + \gamma T_c\,[B_z(x,y,t_{d^{+},k}) - B_z(x,y,t_{d^{-},k})]}{2} \quad \text{(A.12)}$$

In the case that systematic phase artifacts are static, i.e. that δ is unaffected by drift or intrinsic neural-activity related magnetic fields, these expressions become

$$\phi_{d,k}(x,y,z,t_{d^{\pm},k}) = \gamma T_c\,[B_z(x,y,t_{d^{+},k}) + B_z(x,y,t_{d^{-},k})] \quad \text{(A.13)}$$

and

$$\phi_{d,k}^{AVG}\,(x,y,t_{d^{\pm},k}) = \delta\,(x,y,t_{d^{\pm},k}) + \frac{\gamma T_c[B_z(x,y,t_{d^{+},k}) - B_z(x,y,t_{d^{-},k})]}{2} \quad \text{(A.14)}$$

respectively.

In the analyses in the main study we examined characteristics of $\phi_{NC,k}$, or $\phi_{d,k}$ by examining standard deviations in AP or BK regions of interest, and across different experimental segments. Analysis of $\phi_{NC,k}$ across different segments will test for variations caused by intrinsic magnetic fields alone. Analysis of $\phi_{d,k}$ (or $\phi_{d,k}^{AVG}$) will test for variations possibly caused by tissue conductivity changes. Note that observation of a particular standard deviation in any one of these quantities may not in itself indicate a high level of activity. Even if conductivity distributions are static, they may exhibit large standard deviations only because of sample chamber geometry and the ROI chosen, passive conductivity inhomogeneities or unrelated MR artifacts. However, examining standard deviations across experimental segments while maintaining other factors constant, we would expect larger apparent conductivity variations, and therefore larger integrated B_z variations, in relatively more active tissue (Sadleir et al., 2010).

APPENDIX B – Other Experimental Influences

Comparisons of $\phi_{d,k}$ values across PRE, POST and DEAD segments may be modified by experimental influences other than neuronal conductivity changes. Examples include effects of media dilution caused by control or treatment agent addition, change in cell sizes caused

by treatment agents (when comparing PRE to POST segments); or changes in sample chamber conductivity composition caused by cell death (comparing POST to DEAD segments). Clear comparisons between standard deviations in experiments performed at 100 μA and 1 mA MREIT imaging currents may also be difficult because of ROIs chosen and effects of noise. In the sections below we describe each moderating effect and discuss their implications for comparisons made in this study.

B.1 Dilution effects

Since media volumes surrounding ganglia were approximately doubled upon fluid administration, we would expect that MREIT phase amplitudes and standard deviations in BK compartments would decrease relative to PRE measurements as imaging current flow is distributed into this extra solution in POST and DEAD experimental segments. This would occur because, while current amplitude would be the same before and after solution addition, addition of extra fluid should dilute the current density found in any discrete slice, reducing the resulting phase range. We modeled the effect of dilution on standard deviations of phase images using a passive finite element model with the same dimensions as the sample chamber (COMSOL Multiphysics, Burlington, MA), both when extra control and treatment solution were added. The electric currents module was used, and initial solution conductivity and volume in the chamber was set to be 5.8 S/m. The model was solved subject to a current density of 200 μA applied to one port, with the diametrically opposite port set to a ground voltage. We found a decrease in current density, B_z amplitudes and therefore B_z standard deviations of at most 20% percent when extra ASW was added. The phase amplitude decrease due to treatment (KCl solution conductivity of 6.6 S/m) cases was predicted to be slightly larger (at most 24% percent) because of the higher conductivity of the treatment solution.

B.2 Change in cell size

A decrease in cell sizes, potentially caused by osmotic shock, may result in larger volumes of free fluid in the sample chamber, and therefore affect current distribution within it. We modified the finite element model specified in Appendix B.2 above to include 9 internal ellipsoids, each with an initial 500 μm diameter (transverse semiaxes 250 μm, axial semiaxis 125 μm). The conductivity inside the ellipsoids was set to 3.63 S/m and the bath conductivity was set to be 5.07 S/m (Sadleir et al., 2010). We estimated the effect of 1% and 2.5% reductions in cell diameters on phase standard deviations to determine the potential strength of this factor. Current density data generated from the finite element model was converted to magnetic flux density data at the same resolution as experimental data using a FFT implementation of the Biot-Savart law (Minhas et al., 2011). Standard deviations in B_z within in a central 36 × 36 voxel compartment (2.5 mm × 2.5 mm) containing all 9 ellipsoids were found to be approximately 0.18% smaller when all cell diameters decreased by 1%, and 0.64% smaller if cell diameters decreased by 2.5%. Since these decreases were smaller than experimental increases, we therefore conclude that cell shrinkage, if present, was not a significant physical contributor to observed effects.

APPENDIX C Comparisons of ϕd,kAVG and ϕNC,k Data

As noted in equation A.10, if the conductivity distribution within the sample chamber is static we should recover $\delta(x,y,t_{NC,k})=\phi_{d,k}^{AVG}(x,y,t_{d^{\pm},k})$. This should be observed in BK ROIs for all experimental segments. We performed this test for the 12 animals in the 1 mA experiments of this study. Because averaging involves reduction in noise by a factor of 1/√2, comparisons of standard deviations in NC and averaged MREIT data within experimental segments were made after multiplying MREIT standard deviations by a factor of √2. Within individual segments (k = PRE, POST or DEAD) we compared, in turn, standard deviations in $\boldsymbol{\phi}_{NC,k}$ data to $\phi_{1,k}^{AVG}$, $\boldsymbol{\phi}_{NC,k}$ data to $\phi_{2,k}^{AVG}$, and $\phi_{1,k}^{AVG}$ to $\phi_{2,k}^{AVG}$, to verify (A.10). Results of the comparison are shown in Table C.1 below. No significant difference was found, confirming the hypothesis. We would expect that similar comparisons between AP compartments using this analysis may recover significant differences because of the non-static conductivity distribution. Results are not presented here but may be the focus of subsequent analysis.

Table C.1

Tabulated p-values comparing averaged MREIT data and NC data within each experimental segment for 1 mA experiments. Averaged MREIT standard deviation data were multiplied by √2 before comparisons.

Comparison Experimental Phase *k*	$\boldsymbol{\phi}_{NC,k}$ to $\phi_{1,k}^{AVG}$	$\boldsymbol{\phi}_{NC,k}$ to $\phi_{2,k}^{AVG}$	$\phi_{1,k}^{AVG}$ to $\phi_{2,k}^{AVG}$
PRE	0.787	0.828	0.626
POST	0.975	0.880	0.855
DEAD	0.634	0.326	0.613

Equation A.10 can further be used to verify MREIT measurements, that is, to show that MREIT experimental data agree with assumptions. This may be done by fitting regression lines between NC and averaged data, or between sets of averaged data. Ideally, AVG and NC data should be identical and regression lines should have a slope of one and offset of zero. However, Deming regression (Cornbleet and Gochman, 1979; Kelly, 1984) must be used, because ordinary least squares regression (OLS) is not appropriate when both variables have noise. DEAD images were used since A.10 should apply for these cases. Deming fits between NC and AVG data were modified to account for their different variances, as noted in the analysis above. We tested that the slope of regression lines fitted by Deming regression was identity when comparing $\boldsymbol{\phi}_{NC,DEAD}$ against $\phi_{1,DEAD}^{AVG}$; $\boldsymbol{\phi}_{NC,DEAD}$ against $\phi_{2,DEAD}^{AVG}$; and $\phi_{1,DEAD}^{AVG}$ against $\phi_{2,DEAD}^{AVG}$ data, for both AP and BK ROIs. Below, we show an example of the fit between $\boldsymbol{\phi}_{NC,DEAD}$ and $\phi_{2,DEAD}^{AVG}$ for the AP ROI of Aplysia 14. In this case, the slope of the line was 0.984. (n=255, [0.716, 1.25] 95% CI) and the offset of the line was -0.005 ([-0.018, 0.013] 95% CI). The p-value for this line having a slope of 1 was 0.9081, and the p-value for zero offset was 0.5611. Similar relationships were found between all slope comparisons in AP and BK compartments.

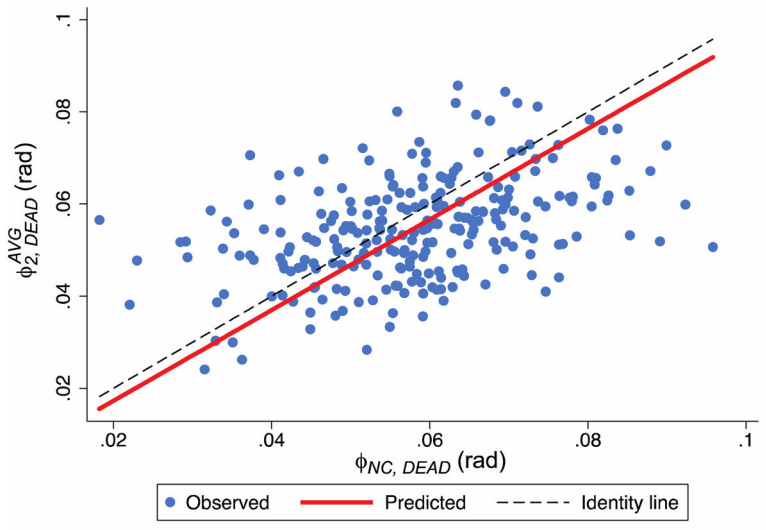

Figure C.1.

Scatterplot of NC DEAD data ($\phi_{NC,DEAD}$) against $\phi^{AVG}_{2,DEAD}$ for Aplysia 14 in the AP ROI. Also plotted on this graph is the identity line predicted by equation A.10.

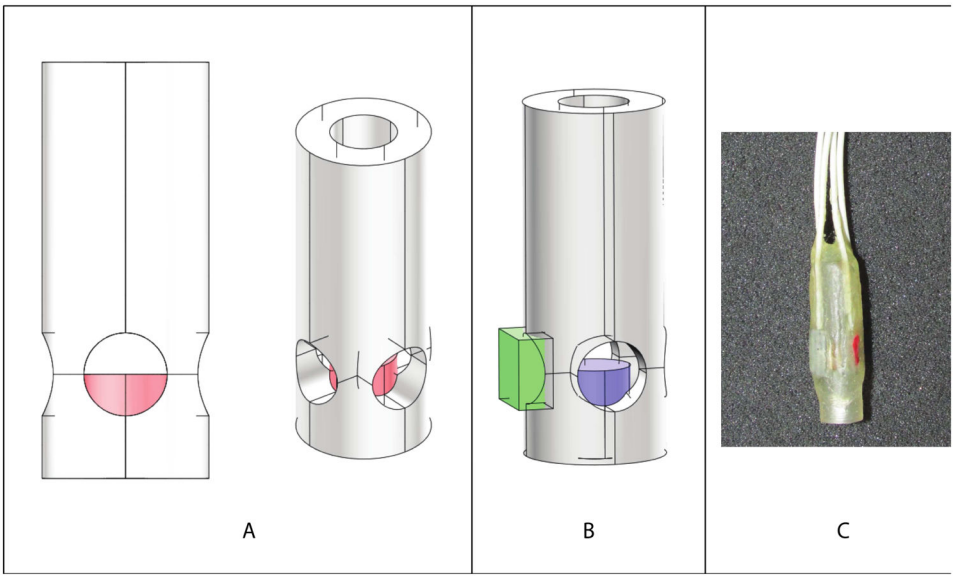

Figure 1.

Test chamber geometry and photograph. (A) shows coronal and oblique views of test chamber. Port diameters were approximately 2 mm. (B) shows a single hydrogel electrode over one port and (C) shows the actual test chamber. Each of the four port wires were connected to a customized MREIT current source located outside the magnet bore.

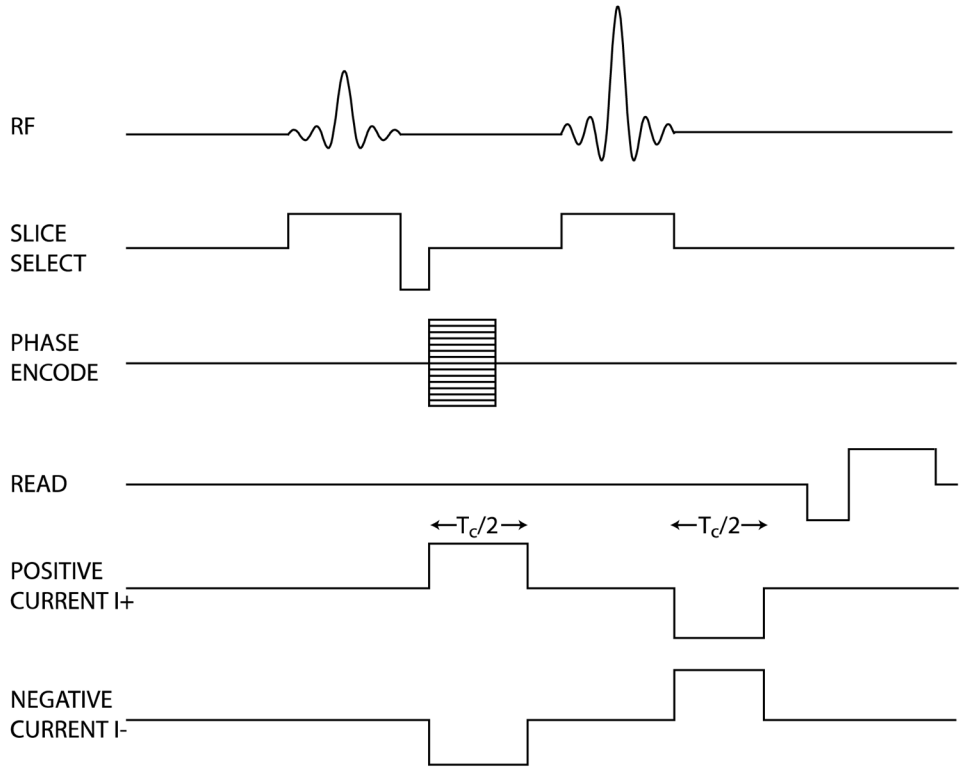

Figure 2.

Spin-echo pulse sequence, after Scott et al. (1991). The total imaging time was determined as TR x PE x NAV. In all experiments, TR was 330 ms, PE was 128, NAV was 8. Thus, the total imaging time for each current configuration was 338 s. Phase data from both '+' (positive current first, then an equal amplitude negative current after the refocusing 180° RF pulse) and '-' current scans were collected separately, then subtracted to remove systematic phase artifact and double signal amplitude for MREIT data sets. NC data were acquired from single scans.

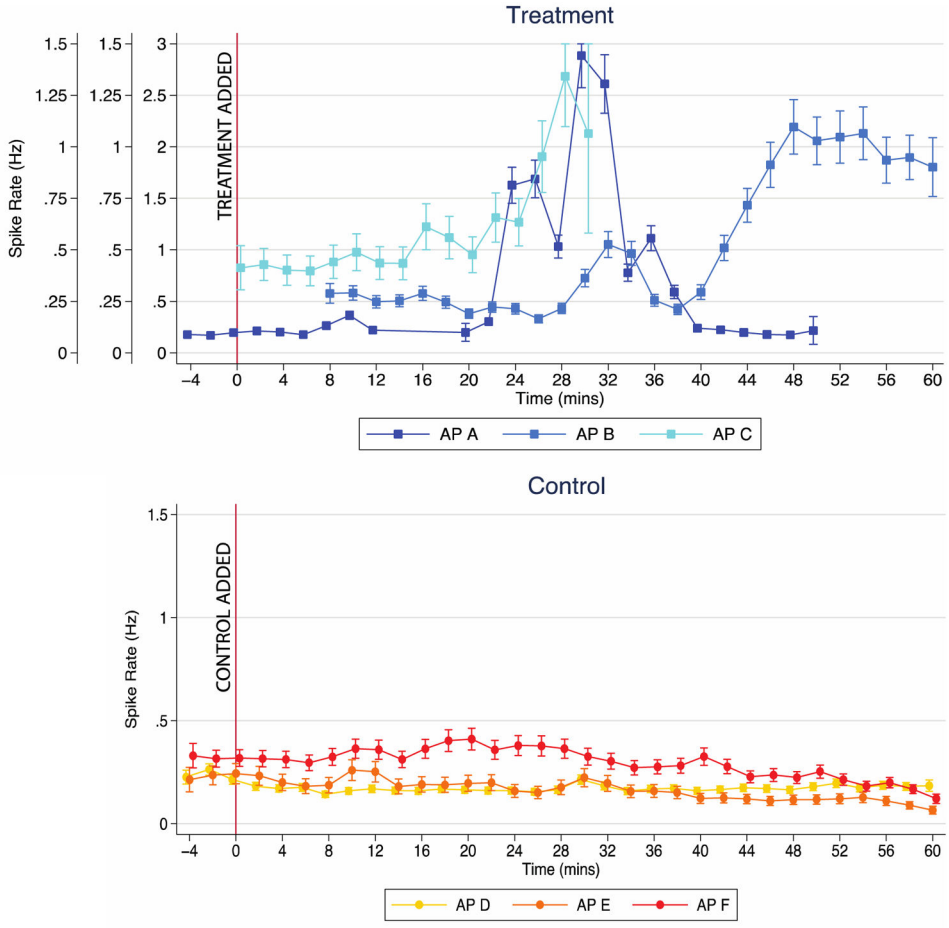

Figure 3.

Results of averaged MEA recording and spike detection relative to time of treatment administration for six ganglion samples (not represented in MREIT data): three treatment (AP A, B and C, and three controls (AP D, E and F). Timing is shown relative to time of treatment administration. 95% confidence intervals are shown on average spike rates. Scale for AP A is 0–3 Hz.

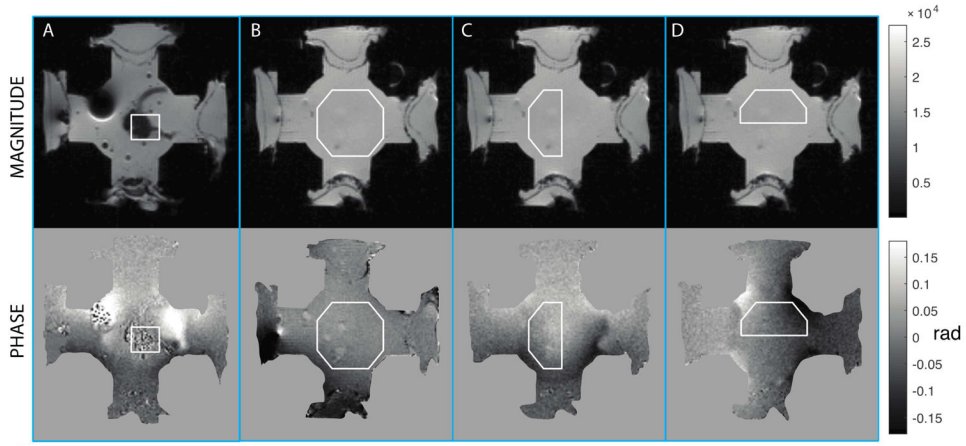

Figure 4.

Example transverse images of Aplysia 18. In each panel, the top image shows magnitude and the bottom image displays phase component (ϕ_1). (A) AP slice (slice 4), showing outline of AP compartment (B) BK slice (slice 7), showing outline of NC region of interest, (C) BK slice (slice 7), showing current I_1 region of interest, and (D) BK slice (slice 7) showing current I_2 region of interest.

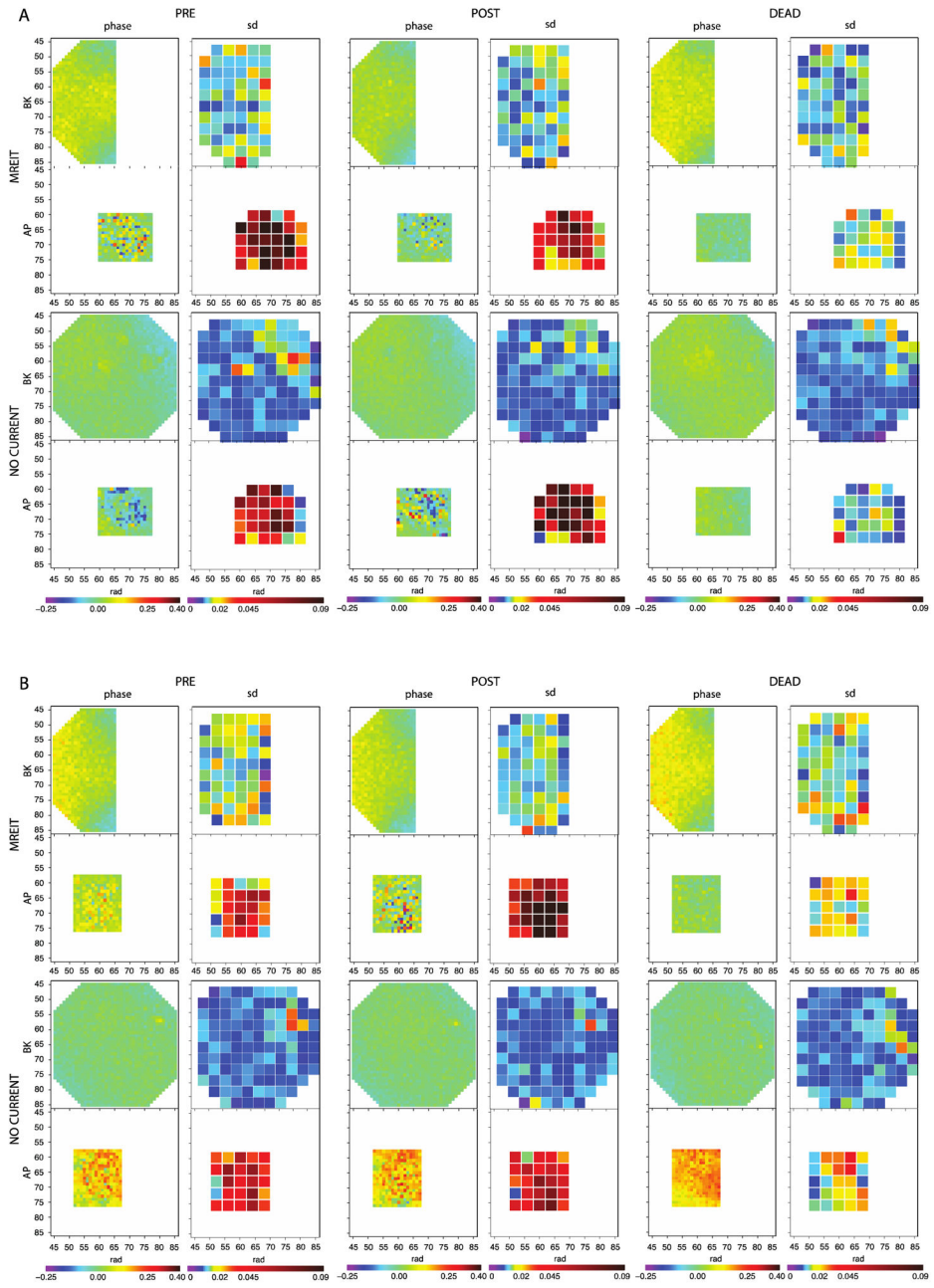

Figure 5.

Examples of MREIT and NC phase and phase standard deviation (sd) samples, shown here for A) control (Aplysia 18) and B) treatment (Aplysia 12) animals. MREIT data for AP and BK compartments (current direction I_1 only) are shown in PRE, POST and DEAD phases in the top two rows, and corresponding NC data are shown in the bottom two rows. Standard deviation samples were formed from raw phase data as described in Section 2.9.

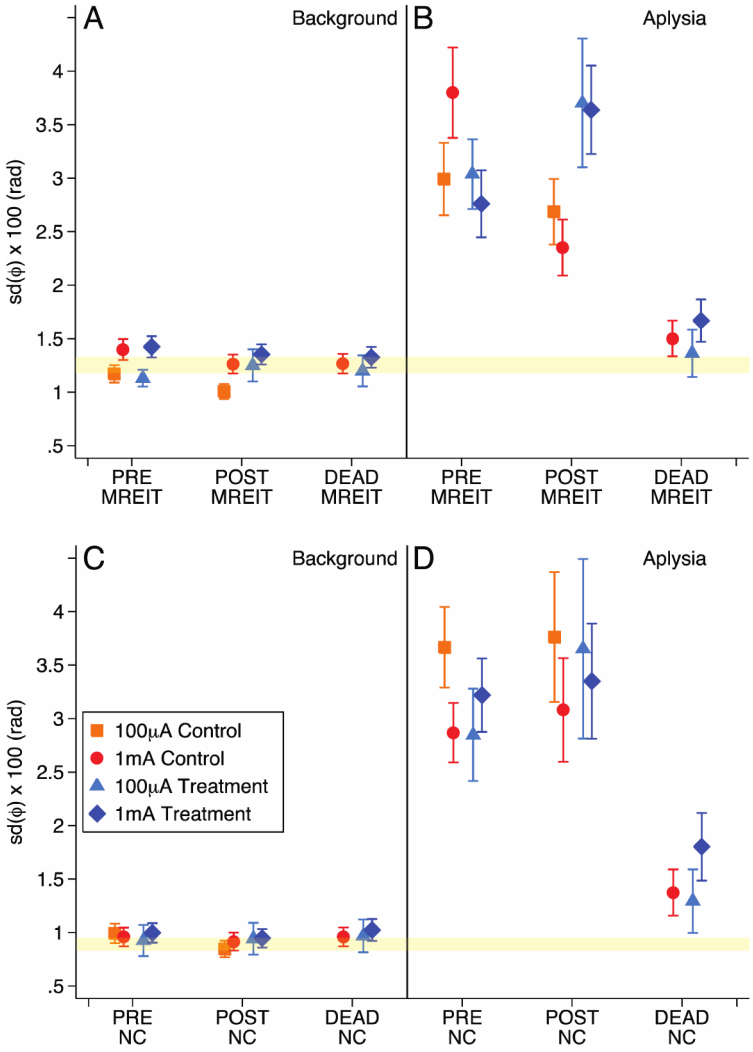

Figure 6.

Plot showing standard deviations, with 95% confidence intervals estimated via linear regression, in BK or AP regions using NC (0 mA) 100 μA or 1 mA imaging before (PRE), after (POST) and long after (DEAD) treatment or control administrations. In this figure, 'NC' data are distinguished by experimental group (1 mA or 100 μA, control or treatment). Standard deviations are shown for PRE, POST and DEAD conditions for (A) BK MREIT data, (B) AP MREIT data, (C) BK NC data and (D) AP NC data. Confidence intervals for baseline noise are shaded on both NC and MREIT panels in yellow.

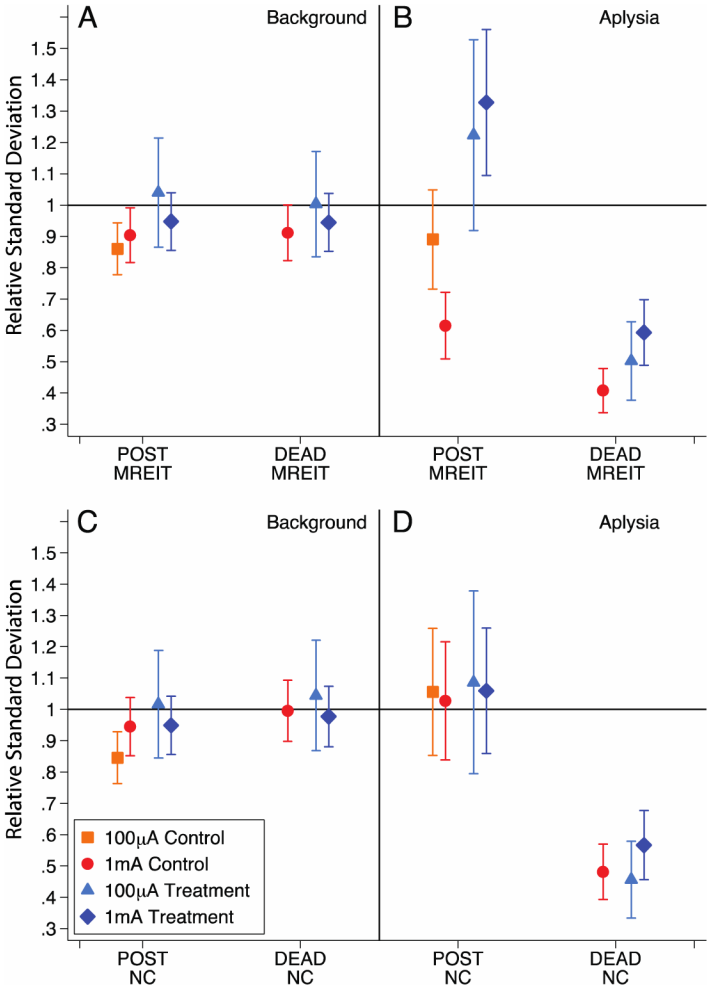

Figure 7.

Plot showing RSDs, with 95% confidence intervals estimated via linear regression, in BK or AP regions using NC (0 mA) 100 μA or 1 mA imaging of the ratio of standard deviations after (POST) and long after (DEAD) to those measured before (PRE) treatment or control administrations. In this figure, 'NC' data are distinguished by experimental group (1 mA or 100 μA, control or treatment). Standard deviations are shown for POST/PRE and DEAD/PRE conditions for (A) BK MREIT data, (B) AP MREIT data, (C) BK NC data and (D) AP NC data.

Table 1

MR measurement protocol, including PRE, POST and DEAD conditions, and individual current direction scans.

EXPERIMENTAL SEGMENT	SCAN #	DESCRIPTION	TIME	DATA SET	DATA SET #
PRE	1	NO CURRENT	338 s	PRE NC	1
	2	I_1 +	338 s	PRE I_1	2
	3	I_1 −	338 s		
	4	I_2 +	338 s	PRE I_2	3
	5	I_2 −	338 s		
INTERVENTION		KCL (TREATMENT) or ASW (CONTROL)	10 min		
		WAIT	20 min		
POST	6	NO CURRENT	338 s	POST NC	4
	7	I_1 +	338 s	POST I_1	5
	8	I_1 −	338 s		
	9	I_2 +	338 s	POST I_2	6
	10	I_2 −	338 s		
		WAIT	19 hr		
DEAD	11	NO CURRENT	338 s	DEAD NC	7
	12	I_1 +	338 s	DEAD I_1	8
	13	I_1 −	338 s		
	14	I_2 +	338 s	DEAD I_2	9
	15	I_2 −	338 s		

Table 2

MREIT Data collection notes.

Animal	Current	Treatment/Control	AP slice	BK Slice	Remarks
7	1 mA	Treatment	5	8	
9	1 mA	Treatment	4	8	
10	1 mA	Treatment	4	8	
11	1 mA	Treatment	4	7	DEAD NC data lost
12	1 mA	Treatment	4	7	
13	1 mA	Treatment	4	8	DEAD I_2 data lost
8	1 mA	Control	4	8	
14	1 mA	Control	4	6	
15	1 mA	Control	5	7	
16	1 mA	Control	4	7	
17	1 mA	Control	4	6	
18	1 mA	Control	4	7	
19	100 μA	Treatment	5	7	Only PRE had current 8 average scans
20	100 μA	Treatment	5	7	Only PRE had current 8 average scans POST I_2 data lost
21	100 μA	Treatment	4	9	Only PRE had current 8 average scans
22	100 μA	Treatment	5	7	Only PRE had current 8 average scans
25	100 μA	Treatment	4,5	7	
26	100 μA	Treatment	5	9	
30	100 μA	Control	4	7	Insufficient over-night waiting time
31	100 μA	Control	3	6	Insufficient over-night waiting time
32	100 μA	Control	4	5	Insufficient over-night waiting time
33	100 μA	Control	3	7	Insufficient over-night waiting time
34	100 μA	Control	3	6	DEAD data lost
35	100 μA	Control	3	7	Insufficient over-night waiting time

Table 3

MREIT Median (and count) of Standard Deviation (x 100) in phase for background and ganglion ROIs by Treatment, Current amount and Current direction.

			Treatment				Control			
			100 μA		1 m A		100 μA		1 m A	
	Timing	Direction	NC	Current	NC	Current	NC	Current	NC	Current
Background										
1	PRE	None	0.95 (207)		1.01 (600)		0.97 (584)		0.96 (578)	
2		I_1		1.17 (355)		1.51 (330)		1.23 (366)		1.39 (359)
3		I_2		1.16 (355)		1.48 (328)		1.14 (366)		1.45 (338)
4	POST	None	0.96 (207)		0.96 (600)		0.87 (648)		0.92 (636)	
5		I_1		1.20 (119)		1.36 (330)		1.04 (366)		1.30 (359)
6		I_2		1.32 (112)		1.42 (328)		1.06 (366)		1.34 (338)
7	DEAD	None	0.97 (207)		1.03 (504)				0.96 (605)	
8		I_1		1.21 (119)		1.43 (330)				1.27 (318)
9		I_2		1.27 (115)		1.34 (271)				1.31 (310)
Aplysia										
1	PRE	None	3.17 (65)		3.26 (130)		4.25 (142)		3.14 (164)	
2		I_1		2.86 (145)		3.03 (130)		3.45 (142)		4.49 (164)
3		I_2		2.93 (145)		2.88 (130)		3.19 (142)		3.63 (164)
4	POST	None	3.53 (65)		3.77 (130)		4.31 (137)		2.93 (164)	
5		I_1		3.95 (65)		4.04 (130)		3.19 (137)		2.36 (164)
6		I_2		3.86 (65)		3.83 (130)		3.03 (137)		2.27 (164)
7	DEAD	None	1.30 (65)		1.88 (111)				1.32 (164)	
8		I_1		1.44 (65)		1.73 (130)				1.49 (164)
9		I_2		1.50 (65)		1.71 (107)				1.55 (164)

Table 4

MREIT Median (and count) of RSD in phase for background and ganglion by Treatment, Current amount and Current direction.

			Treatment				Control			
			100 μA		1 m A		100 μA		1 m A	
	Timing	Direction	NC	Current	NC	Current	NC	Current	NC	Current
Background										
4	POST	None	1.00 (207)		0.95 (600)		0.86 (584)		0.94 (578)	
5		I_1		0.98 (119)		0.95 (330)		0.85 (366)		0.93 (359)
6		I_2		1.08 (112)		0.96 (328)		0.89 (366)		0.93 (338)
7	DEAD	None	1.03 (207)		0.98 (504)				1.01 (578)	
8		I_1		1.01 (119)		0.97 (330)				0.93 (318)
9		I_2		1.01 (115)		0.93 (271)				0.92 (305)
Aplysia										
4	POST	None	1.14 (65)		1.05 (130)		1.00 (125)		1.00 (164)	
5		I_1		1.27 (65)		1.27 (130)		0.90 (125)		0.60 (164)
6		I_2		1.19 (65)		1.20 (130)		0.87 (125)		0.66 (164)
7	DEAD	None	0.44 (65)		0.56 (111)				0.43 (164)	
8		I_1		0.44 (65)		0.57 (130)				0.33 (164)
9		I_2		0.49 (65)		0.59 (107)				0.43 (164)